Article:
Wang, Y, Jimack, PK and Walkley, MA orcid.org/0000-0003-2541-4173 (2019) Energy Analysis for the One-Field Fictitious Domain Method for Fluid-Structure Interactions. Applied Numerical Mathematics, 140. pp. 165-182. ISSN 0168-9274

https://doi.org/10.1016/j.apnum.2019.02.003

Energy analysis for the one-field fictitious domain method for fluid-structure interactions

Yongxing Wang*, Peter K. Jimack, Mark A. Walkley

School of Computing, University of Leeds, Leeds, UK, LS2 9JT

Abstract

In this article, the energy stability of a one-field fictitious domain method is proved and validated by numerical tests in two and three dimensions. The distinguishing feature of this method is that it only solves for one velocity field for the whole fluid-structure domain; the interactions remain decoupled until solving the final linear algebraic equations. To achieve this the finite element procedures are carried out separately on two different meshes for the fluid and solid respectively, and the assembly of the final linear system brings the fluid and solid parts together via an isoparametric interpolation matrix between the two meshes. The weak formulations are introduced in the continuous case and after discretization in time. Then the stability is analyzed through an energy estimate. Finally, numerical examples are presented to validate the energy stability properties.

Keywords: fluid structure, finite element, fictitious domain, energy stable, immersed finite element, one field, monolithic scheme, Eulerian formulation.

1. Introduction

Fluid-Structure Interaction (FSI) problems are common in many areas. For most FSI problems, analytical solutions of the controlling equations are impossible to obtain, whereas laboratory experiments are complex, expensive and limited in scope. Therefore, numerical simulations play an important role in order to understand the fundamental physics involved in the complex interaction between fluids and structures.

In a previous study [1], we present a one-field Fictitious Domain Method (FDM) which only solves for one velocity field and one pressure field in the whole domain, based upon the finite element interpolation. This one-field FDM approach is related to the Immersed Finite Element Method (IFEM) but differs in at least one important respect: the classical IFEM does not solve the solid

*Corresponding author

Email address: jungsirwang@gmail.com/scsywan@leeds.ac.uk (Yongxing Wang)

equation [2–6]. Instead, the solid information is arranged on the right-hand side of the fluid equation as a prescribed force. The one-field FDM solves the solid equation together with the fluid equation in one discretized linear algebraic system. The similarity is that both methods only solve for velocity and pressure fields (no solid displacement). Other FDM techniques exist but are typically based upon the use of a Discrete Lagrange Multiplier (DLM): such methods [7–12] solve the solid equation, but for a displacement field, and couple this displacement with the velocity of the fictitious fluid via a Lagrange multiplier. This leads to a large discretized linear algebra system. The one-field FDM rewrites the solid equation in terms of a velocity variable and couples the fictitious fluid through a finite element interpolation. Monolithic Eulerian methods [13, 14] also express the solid equation in terms of velocity, and the fluid and solid are coupled naturally on an interface-fitted mesh. The one-field FDM uses two meshes to represent the fluid and solid respectively, and the FEM isoparametric interpolation is adopted to transfer information between the two meshes. Consequently, before discretization in space, these two methods have many similarities, the advantage of the one-field FDM being that interface fitting is not required. We find that the advantages of using the FEM interpolation function are: improved accuracy compared with methods such as the discrete delta function or RKPM (Reproducing Kernel Particle Method); effective interpolation of the velocity field through the use of quadratic elements; and effectively capturing the density jumps when using a lumped mass matrix.

There are also other Eulerian formulations for FSI problems: [15] uses the level set method to capture the fluid-structure interface, and a Lagrangian multiplier and penalty method to couple the fluid and solid. [16–20] use an Initial Points Set to capture the fluid-structure interface. After getting the position of the interface, [16–19] use a characteristic function to smooth stress and velocity across the interface. Alternatively [20, 21] modify the local finite elements in order to capture jumps sharply, and [22, 23] use an XFEM-like method to enrich the shape functions locally in order to capture the discontinuity.

The main developments in this paper, following from [1], are as follows. The exact energy-preserving property in the continuous case is proved. The energy-stability property after time discretization is proved, and the same property is also proved after spatial discretization. The implementation in this paper is based on an $\mathbf{F}$-scheme, i.e., the solid deformation tensor $\mathbf{F}$ is updated (see section 4), while the previous paper uses a $\boldsymbol{\sigma}$-scheme (see equation (29) in [1]). The methodology and analysis is demonstrated to extend to the three-dimensional case.

The paper is organized as follows. Control equations and weak formulation are introduced in section 2 and 3 respectively. The time discretized weak form is then presented in section 4. Stability of the proposed scheme is analyzed in section 5. Space discretization is discussed in section 6. Numerical examples are given in section 7, and conclusions are presented in section 8.

2. Control equations

In the following context, $\Omega_t^f \subset \mathbb{R}^d$ and $\Omega_t^s \subset \mathbb{R}^d$ with $d = 2, 3$ denote the fluid and solid domain respectively which are time dependent regions as shown in Figure 1. $\Omega = \Omega_t^f \cup \Omega_t^s$ is a fixed domain (with outer boundary Γ) and $\Gamma_t = \partial\Omega_t^f \cap \partial\Omega_t^s$ is the moving interface between fluid and solid. We denote by $\mathbf{X}$ the reference (material) coordinates of the solid, by $\mathbf{x} = \mathbf{x}(\cdot, t)$ the current coordinates of the solid, and by $\mathbf{x}_0$ the initial coordinates of the solid.

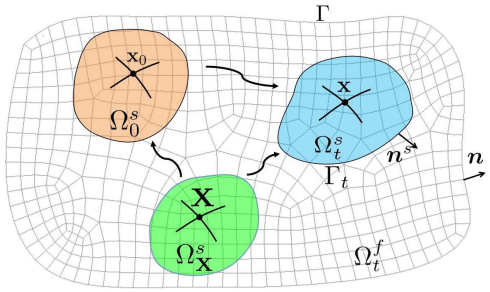

Figure 1: Schematic diagram of FSI, $\Omega = \Omega_t^f \cup \Omega_t^s$.

Let $\rho, \mu, \mathbf{u}, p, \boldsymbol{\sigma}$ denote the density, viscosity, velocity, pressure and stress tensor respectively. We assume both an incompressible fluid and incompressible solid, then the conservation of momentum and conservation of mass take the same form as follows:

Momentum equation:

$$\rho \frac{d\mathbf{u}}{dt} = \nabla \cdot \boldsymbol{\sigma}, \tag{1}$$

Continuity equation:

$$\nabla \cdot \mathbf{u} = 0. \tag{2}$$

An incompressible Newtonian constitutive equation in Ω^f can be expressed as:

$$\boldsymbol{\sigma} = \boldsymbol{\sigma}^f = \mu^f \mathrm{D}\mathbf{u}^f - p^f \mathbf{I}, \tag{3}$$

where $\mathrm{D}\mathbf{u} = \nabla\mathbf{u} + \nabla^T\mathbf{u}$. We shall consider an incompressible viscous neo-Hookean solid in Ω_t^s [8], in which case the Cauchy stress tensor is composed of an elastic part and a viscous part:

$$\boldsymbol{\sigma} = \boldsymbol{\sigma}^s = \boldsymbol{\sigma}_e^s + \boldsymbol{\sigma}_v^s, \tag{4}$$

with

$$\boldsymbol{\sigma}_e^s = c_1 J^{-1} \left(\mathbf{F}\mathbf{F}^T - \mathbf{I}\right) - p^s \mathbf{I}, \tag{5}$$

and

$$\boldsymbol{\sigma}_v^s = \mu^s \mathrm{D}\mathbf{u}^s. \tag{6}$$

In the above, $\mathbf{F} = \frac{\partial \mathbf{x}}{\partial \mathbf{X}} = \frac{\partial \mathbf{x}}{\partial \mathbf{x}_0}\frac{\partial \mathbf{x}_0}{\partial \mathbf{X}} = \nabla_0 \mathbf{x} \nabla_{\mathbf{X}} \mathbf{x}_0$ is the deformation tensor of the solid, and $J = det\mathbf{F}$ is the determinant of $\mathbf{F}$. Finally the system is complemented with the following boundary and initial conditions.

$$\mathbf{u}^f = \mathbf{u}^s \quad on \quad \Gamma_t, \tag{7}$$

$$\mathbf{n}^s \boldsymbol{\sigma}^f = \mathbf{n}^s \boldsymbol{\sigma}^s \quad on \quad \Gamma_t, \tag{8}$$

$$\mathbf{u}^f = \mathbf{0} \quad on \quad \Gamma, \tag{9}$$

$$\mathbf{u}^f\big|_{t=0} = \mathbf{u}_0^f, \tag{10}$$

$$\mathbf{u}^s\big|_{t=0} = \mathbf{u}_0^s. \tag{11}$$

Other boundary conditions are possible on Γ but (9) are used here for simplicity.

Remark 1. *It may be possible to absorb the term $-c_1 J^{-1}$ into p^s as well (see [8]). In this case, the solid is not stress free, and one creates a jump of the pressure across the fluid-solid interface if the fluid is stress free. This does not matter if the discontinuity of pressure can be exactly captured, such as an interface-fitted method with discontinuous element for pressure. However, for the interface-unfitted methods, adopted in this paper, it is wiser to include $-c_1 J^{-1}$ in the constitutive equation. In this case, the corresponding energy function for the hyperelastic stress in (4) is defined by [10]:*

$$\Psi(\mathbf{F}) = \frac{c_1}{2}\left(tr_{\mathbf{F}\mathbf{F}^T} - d\right) - c_1 ln(J). \tag{12}$$

Remark 2. *In the continuous case $J = 1$ exactly holds for an incompressible material, therefore the term $ln(J)$ is zero in (12). However for the numerical methods using two meshes, $J = 1$ cannot be guaranteed. Furthermore, the energy function (12) is also consistent with the constitutive equation (5). Notice that the following energy function and constitutive equation are consistent with each other:*

$$\Psi(\mathbf{F}) = \frac{c_1}{2}\left(tr_{\mathbf{F}\mathbf{F}^T} - d\right), \tag{13}$$

and

$$\boldsymbol{\sigma}_e^s = c_1 J^{-1} \mathbf{F}\mathbf{F}^T - p^s \mathbf{I}. \tag{14}$$

3. Weak formulation

The finite element weak form discussed in this section is almost the same as that in [1], the only difference is that we integrate the solid stress in the reference domain, because we shall update the deformation tensor (**F**-scheme) rather than the solid stress as done in [1] ($\boldsymbol{\sigma}$-scheme). In the following context, let $L^2(\omega)$ be the square integrable functions in domain ω, endowed with norm

$\|u\|_{0,\omega}^2 = \int_\omega |u|^2$ ($u \in L^2(\omega)$). Let $H^1(\omega) = \left\{u : u, \nabla u \in L^2(\omega)\right\}$ with the norm denoted by $\|u\|_{1,\omega}^2 = \|u\|_{0,\omega}^2 + \|\nabla u\|_{0,\omega}^2$. We also denote by $H_0^1(\omega)$ the subspace of $H^1(\omega)$ whose functions have zero values on the boundary of ω, and denote by $L_0^2(\omega)$ the subspace of $L^2(\omega)$ whose functions have zero mean value.

Let $p = \begin{cases} p^f & in \quad \Omega^f \\ p^s & in \quad \Omega_t^s \end{cases}$. Given $\mathbf{v} \in H_0^1(\Omega)^d$, we perform the following symbolic operations:

$$\int_{\Omega_t^f} \text{Eq.}(1) \cdot \mathbf{v} d\mathbf{x} + \int_{\Omega_t^s} \text{Eq.}(1) \cdot \mathbf{v} d\mathbf{x}.$$

Integrating the stress terms by parts, the above operations, using constitutive equation (3) and (4) and boundary condition (8), gives:

$$\begin{aligned} &\rho^f \int_\Omega \frac{d\mathbf{u}}{dt} \cdot \mathbf{v} d\mathbf{x} + \frac{\mu^f}{2} \int_\Omega \mathrm{D}\mathbf{u} : \mathrm{D}\mathbf{v} d\mathbf{x} - \int_\Omega p \nabla \cdot \mathbf{v} d\mathbf{x} \\ &+ \frac{\mu^\delta}{2} \int_{\Omega_t^s} \mathrm{D}\mathbf{u} : \mathrm{D}\mathbf{v} d\mathbf{x} + \rho^\delta \int_{\Omega_t^s} \frac{d\mathbf{u}}{dt} \cdot \mathbf{v} d\mathbf{x} \\ &+ c_1 \int_{\Omega_t^s} J^{-1} \left(\mathbf{F}\mathbf{F}^T - \mathbf{I}\right) : \nabla \mathbf{v} d\mathbf{x} = 0, \end{aligned} \tag{15}$$

where $\rho^\delta = \rho^s - \rho^f$ and $\mu^\delta = \mu^s - \mu^f$. Note that the integrals on the interface Γ_t are cancelled out using boundary condition (8). This is not surprising because they are internal forces for the whole FSI system considered here.

Transforming the integral of the last two terms of (15) to the reference coordinate system, combined with the following symbolic operations for $q \in L^2(\Omega)$,

$$-\int_{\Omega_t^f} \text{Eq.}(2) q d\mathbf{x} - \int_{\Omega_t^s} \text{Eq.}(2) q d\mathbf{x},$$

leads to the weak form of the FSI system as follows.

Problem 1. *Given* $\mathbf{u}_0$ *and* Ω_0^s*, find* $\mathbf{u}(t) \in H_0^1(\Omega)^d$*,* $p(t) \in L_0^2(\Omega)$ *and* Ω_t^s*, such that for* $\forall \mathbf{v} \in H_0^1(\Omega)^d$*,* $\forall q \in L^2(\Omega)$*, the following two equations hold:*

$$\begin{aligned} &\rho^f \int_\Omega \frac{\partial \mathbf{u}}{\partial t} \cdot \mathbf{v} d\mathbf{x} + \rho^f \int_\Omega (\mathbf{u} \cdot \nabla) \mathbf{u} \cdot \mathbf{v} d\mathbf{x} \\ &+ \frac{\mu^f}{2} \int_\Omega \mathrm{D}\mathbf{u} : \mathrm{D}\mathbf{v} d\mathbf{x} - \int_\Omega p \nabla \cdot \mathbf{v} d\mathbf{x} \\ &+ \rho^\delta \int_{\Omega_\mathbf{x}^s} \frac{\mathfrak{d}\mathbf{u}}{\mathfrak{d}t} \cdot \mathbf{v} d\mathbf{X} + \frac{\mu^\delta}{2} \int_{\Omega_t^s} \mathrm{D}\mathbf{u} : \mathrm{D}\mathbf{v} d\mathbf{x} \\ &+ c_1 \int_{\Omega_\mathbf{x}^s} \mathbf{F} : \nabla_\mathbf{X} \mathbf{v} d\mathbf{X} - c_1 \int_{\Omega_t^s} J^{-1} \nabla \cdot \mathbf{v} d\mathbf{x} = 0, \end{aligned} \tag{16}$$

and

$$-\int_\Omega q \nabla \cdot \mathbf{u} d\mathbf{x} = 0. \tag{17}$$

In the above, $\frac{\mathfrak{d}(\cdot)}{\mathfrak{d}t}$ is the time derivative with respect to a frame moving with the solid velocity $\mathbf{u}^s = \mathbf{u}|_{\Omega_t^s}$.

4. Discretization in time

We use the backward Euler method to discretize Problem 1, and update coordinates of the solid by $\mathbf{x}_{n+1} = \mathbf{x}_n + \Delta t \mathbf{u}_{n+1}$. As a result, $\mathbf{F}$ is updated by $\mathbf{F}_{n+1} = \mathbf{F}_n + \Delta t \nabla_{\mathbf{X}} \mathbf{u}_{n+1}$, and so,

$$\int_{\Omega_{\mathbf{X}}^s} \mathbf{F}_{n+1} : \nabla_{\mathbf{X}} \mathbf{v} = \int_{\Omega_{\mathbf{X}}^s} \mathbf{F}_n : \nabla_{\mathbf{X}} \mathbf{v} + \Delta t \int_{\Omega_{\mathbf{X}}^s} \nabla_{\mathbf{X}} \mathbf{u}_{n+1} : \nabla_{\mathbf{X}} \mathbf{v}. \tag{18}$$

Using equation (18), the discretized weak form corresponding to Problem 1 may be expressed as:

Problem 2. *Given $\mathbf{u}_n$, p_n and Ω_n^s, find $\mathbf{u}_{n+1} \in H_0^1(\Omega)^d$, $p_{n+1} \in L_0^2(\Omega)$ and Ω_{n+1}^s, such that for $\forall \mathbf{v} \in H_0^1(\Omega)^d$, $\forall q \in L^2(\Omega)$, the following four relations hold:*

$$\begin{aligned}
&\rho^f \int_\Omega \frac{\mathbf{u}_{n+1} - \mathbf{u}_n}{\Delta t} \cdot \mathbf{v} d\mathbf{x} + \rho^f \int_\Omega (\mathbf{u}_{n+1} \cdot \nabla) \mathbf{u}_{n+1} \cdot \mathbf{v} d\mathbf{x} \\
&+ \frac{\mu^f}{2} \int_\Omega \mathrm{D}\mathbf{u}_{n+1} : \mathrm{D}\mathbf{v} d\mathbf{x} - \int_\Omega p_{n+1} \nabla \cdot \mathbf{v} d\mathbf{x} \\
&+ \rho^\delta \int_{\Omega_{\mathbf{X}}^s} \frac{\mathbf{u}_{n+1} - \mathbf{u}_n}{\Delta t} \cdot \mathbf{v} d\mathbf{X} + \frac{\mu^\delta}{2} \int_{\Omega_{n+1}^s} \mathrm{D}\mathbf{u}_{n+1} : \mathrm{D}\mathbf{v} d\mathbf{x} \\
&+ c_1 \Delta t \int_{\Omega_{\mathbf{X}}^s} \nabla_{\mathbf{X}} \mathbf{u}_{n+1} : \nabla_{\mathbf{X}} \mathbf{v} d\mathbf{X} \\
&- c_1 \int_{\Omega_{n+1}^s} J_{n+1}^{-1} \nabla \cdot \mathbf{v} d\mathbf{x} = -c_1 \int_{\Omega_{\mathbf{X}}^s} \mathbf{F}_n \nabla_{\mathbf{X}} \mathbf{v} d\mathbf{X},
\end{aligned} \tag{19}$$

$$- \int_\Omega q \nabla \cdot \mathbf{u}_{n+1} d\mathbf{x} = 0, \tag{20}$$

$$\Omega_{n+1}^s = \{\mathbf{x} : \mathbf{x} = \mathbf{x}_n + \Delta t \mathbf{u}_{n+1}, \mathbf{x}_n \in \Omega_n^s\}, \tag{21}$$

and

$$\mathbf{F}_{n+1} = \mathbf{F}_n + \Delta t \nabla_{\mathbf{X}} \mathbf{u}_{n+1}. \tag{22}$$

A fixed-point iteration will be used at each time step to construct Ω_{n+1}^s implicitly.

5. Stability by energy estimate

5.1. Energy conservation in the continuous case

In this section we shall prove that the weak forms (16) and (17), associated with Problem 1, preserve energy.

Lemma 3. *The energy function $\Psi(\mathbf{F})$ for the hyperelastic stress satisfies:*

$$c_1 \int_0^t \int_{\Omega_{\mathbf{X}}^s} \mathbf{F} : \nabla_{\mathbf{X}} \mathbf{u} d\mathbf{X} - c_1 \int_0^t \int_{\Omega_t^s} J^{-1} \nabla \cdot \mathbf{u} d\mathbf{x} = \int_{\Omega_{\mathbf{X}}^s} \Psi(\mathbf{F}) \mathbf{d}\mathbf{X}. \tag{23}$$

Proof. Since $\frac{\partial tr_{\mathbf{F}\mathbf{F}^T}}{\partial \mathbf{F}} = 2\mathbf{F}$ and $\frac{\partial (det_{\mathbf{F}})}{\partial \mathbf{F}} = det_{\mathbf{F}} \mathbf{F}^{-T}$. Using the fact that $\mathbf{A} : \mathbf{B} = tr_{\mathbf{A}\mathbf{B}^T}$ ($\mathbf{A}$ and $\mathbf{B}$ are arbitrary matrices), we have:

$$\begin{aligned}
&\frac{d}{dt} \int_{\Omega_{\mathbf{X}}^s} \Psi(\mathbf{F}) d\mathbf{X} = \int_{\Omega_{\mathbf{X}}^s} \frac{\partial \Psi}{\partial \mathbf{F}} : \frac{d\mathbf{F}}{dt} d\mathbf{X} \\
=& c_1 \int_{\Omega_{\mathbf{X}}^s} \left(\mathbf{F} - \mathbf{F}^{-T} \right) : \frac{d}{dt} \left(\mathbf{I} + \nabla_{\mathbf{X}} \mathbf{d} \right) d\mathbf{X} \\
=& c_1 \int_{\Omega_{\mathbf{X}}^s} \mathbf{F} : \nabla_{\mathbf{X}} \mathbf{u} d\mathbf{X} - c_1 \int_{\Omega_t^s} J^{-1} \nabla \cdot \mathbf{u} d\mathbf{x},
\end{aligned}$$

where $\mathbf{d}$ is displacement of the solid at time t. □

Lemma 4. *If $(\mathbf{u}, p)$ is the solution pair of Problem 1, then*

$$\int_\Omega (\mathbf{u} \cdot \nabla) \mathbf{u} \cdot \mathbf{u} d\mathbf{x} = 0. \tag{24}$$

Proof. First,

$$\int_\Omega (\mathbf{u} \cdot \nabla) \mathbf{u} \cdot \mathbf{u} d\mathbf{x} = \int_\Omega \nabla (\mathbf{u} \otimes \mathbf{u}) \cdot \mathbf{u} d\mathbf{x} - \int_\Omega |\mathbf{u}|^2 \nabla \cdot \mathbf{u} d\mathbf{x}. \tag{25}$$

Integrate by parts:

$$\int_\Omega \nabla (\mathbf{u} \otimes \mathbf{u}) \cdot \mathbf{u} d\mathbf{x} = \int_\Gamma |\mathbf{u}|^2 \mathbf{u} \cdot \mathbf{n} - \int_\Omega (\mathbf{u} \cdot \nabla) \mathbf{u} \cdot \mathbf{u} d\mathbf{x}. \tag{26}$$

According to a Sobolev imbedding theorem [24, Theorem 6 in Chapter 5] and the inclusion between L^p spaces ($L^q \subset L^p$ if $p < q$), we know $H^1(\Omega) \subset L^4(\Omega)$ (for both 2D and 3D). Therefore $\mathbf{u} \in L^4(\Omega)$, i.e., $\int_\Omega |\mathbf{u}|^4 d\mathbf{x} < \infty$. That is to say $|\mathbf{u}|^2 \in L^2(\Omega)$. Then we have $\int_\Omega |\mathbf{u}|^2 \nabla \cdot \mathbf{u} = 0$ from (17). We also have $\int_\Gamma |\mathbf{u}|^2 \mathbf{u} \cdot \mathbf{n} = 0$ from the boundary condition (9). Substituting these two equations into (25) and (26) gives equation (24). □

Proposition 5 (Energy Conservation)**.** *Let $(\mathbf{u}, p)$ be the solution pair of Problem 1, then*

$$\begin{aligned}
&\frac{\rho^f}{2} \int_\Omega |\mathbf{u}|^2 d\mathbf{x} + \frac{\mu^f}{2} \int_0^t \int_\Omega \mathrm{D}\mathbf{u} : \mathrm{D}\mathbf{u} d\mathbf{x} + \frac{\mu^\delta}{2} \int_0^t \int_{\Omega_t^s} \mathrm{D}\mathbf{u} : \mathrm{D}\mathbf{u} d\mathbf{x} \\
&+ \frac{\rho^\delta}{2} \int_{\Omega_{\mathbf{X}}^s} |\mathbf{u}|^2 d\mathbf{X} + \int_{\Omega_{\mathbf{X}}^s} \Psi(\mathbf{F}) \mathbf{d}\mathbf{X} = \mathbf{0}.
\end{aligned} \tag{27}$$

Proof. We first let $\mathbf{v} = \mathbf{u}$ in (16) and integrate from time 0 to t, then let $q = p$ in (17) and substitute into (16). Finally we can construct the above equation of energy balance due to Lemma 3 and 4. □

5.2. Stability analysis after time discretization

We next demonstrate a similar energy stability result for Problem 2.

Lemma 6. *The trace function* $\frac{1}{2}tr\left(\mathbf{F}\mathbf{F}^T\right)$ *satisfies:*

$$\frac{1}{2}tr\left(\mathbf{F}_{n+1}\mathbf{F}_{n+1}^T\right)-\frac{1}{2}tr\left(\mathbf{F}_n\mathbf{F}_n^T\right)=\Delta t\mathbf{F}_{n+1}:\nabla_{\mathbf{X}}\mathbf{u}_{n+1}-\frac{\Delta t^2}{2}\left|\nabla_{\mathbf{X}}\mathbf{u}_{n+1}\right|^2, \quad (28)$$

where $|\mathbf{A}|^2=\sum_{ij}a_{ij}^2$ *for an arbitrary matrix* $\mathbf{A}=[a_{ij}]$.

Proof.

$$\begin{aligned}&\mathbf{F}_{n+1}\mathbf{F}_{n+1}^T-\mathbf{F}_n\mathbf{F}_n^T\\=&\mathbf{F}_{n+1}\mathbf{F}_{n+1}^T-\left(\mathbf{F}_{n+1}-\Delta t\nabla_{\mathbf{X}}\mathbf{u}_{n+1}\right)\left(\mathbf{F}_{n+1}-\Delta t\nabla_{\mathbf{X}}\mathbf{u}_{n+1}\right)^T\\=&\Delta t\mathbf{F}_{n+1}\nabla_{\mathbf{X}}^T\mathbf{u}_{n+1}+\Delta t\nabla_{\mathbf{X}}\mathbf{u}_{n+1}\mathbf{F}_{n+1}^T-\Delta t^2\nabla_{\mathbf{X}}\mathbf{u}_{n+1}\nabla_{\mathbf{X}}^T\mathbf{u}_{n+1}.\end{aligned}$$

Lemma 6 holds due to

$$\frac{1}{2}tr\big(\mathbf{F}_{n+1}\mathbf{F}_{n+1}^T-\mathbf{F}_n\mathbf{F}_n^T\big)=\Delta t\cdot tr\left(\mathbf{F}_{n+1}\nabla_{\mathbf{X}}^T\mathbf{u}_{n+1}\right)-\frac{\Delta t^2}{2}\left|\nabla_{\mathbf{X}}\mathbf{u}_{n+1}\right|^2.$$

□

Lemma 7. *The log-determinant function* $ln\left(det\mathbf{F}\right)$ *satisfies:*

$$ln(det\mathbf{F}_{n+1})-ln(det\mathbf{F}_n)\geq\Delta t\nabla\cdot\mathbf{u}_{n+1}-\frac{\Delta t^2}{2}\left|\mathbf{F}_{n+1}^{-1}\nabla_{\mathbf{X}}\mathbf{u}_{n+1}\right|^2.$$

Proof. Use the fact that function $ln(det\mathbf{Y})$ is concave over the set of positive definite matrices [25, Chapter 3]. Let $\mathbf{B}=\mathbf{F}\mathbf{F}^T$, $\mathcal{F}(\mathbf{B})=\frac{1}{2}ln\left(det\mathbf{B}\right)=ln\left(det\mathbf{F}\right)$ and $w(\xi)=\mathcal{F}\left(\mathbf{B}_n+\xi\left(\mathbf{B}_{n+1}-\mathbf{B}_n\right)\right)$, then

$$w'(\xi)=\frac{d\mathcal{F}}{d\mathbf{B}}:\left(\mathbf{B}_{n+1}-\mathbf{B}_n\right)=\frac{1}{2}\left(\mathbf{B}_n+\xi\left(\mathbf{B}_{n+1}-\mathbf{B}_n\right)\right)^{-1}:\left(\mathbf{B}_{n+1}-\mathbf{B}_n\right).$$

According to the property of concave functions, we have $w(1)-w(0)\geq w'(1)$, this is to say:

$$\begin{aligned}&ln(det\mathbf{F}_{n+1})-ln(det\mathbf{F}_n)=\mathcal{F}\left(\mathbf{B}_{n+1}\right)-\mathcal{F}\left(\mathbf{B}_n\right)\\\geq&\frac{1}{2}\mathbf{B}_{n+1}^{-1}:\left(\mathbf{B}_{n+1}-\mathbf{B}_n\right)=\frac{1}{2}tr\left(\mathbf{I}-\mathbf{B}_{n+1}^{-1}\mathbf{B}_n\right)\\=&\frac{1}{2}tr\left(\mathbf{I}-\mathbf{B}_{n+1}^{-1}\left(\mathbf{F}_{n+1}-\Delta t\nabla_{\mathbf{X}}\mathbf{u}_{n+1}\right)\left(\mathbf{F}_{n+1}^T-\Delta t\nabla_{\mathbf{X}}^T\mathbf{u}_{n+1}\right)\right)\\=&\frac{\Delta t}{2}tr\left(\mathbf{F}_{n+1}^{-T}\nabla_{\mathbf{X}}^T\mathbf{u}_{n+1}+\mathbf{F}_{n+1}^{-T}\mathbf{F}_{n+1}^{-1}\nabla_{\mathbf{X}}\mathbf{u}_{n+1}\mathbf{F}_{n+1}^T\right)\\&-\frac{\Delta t^2}{2}tr\left(\mathbf{F}_{n+1}^{-T}\mathbf{F}_{n+1}^{-1}\nabla_{\mathbf{X}}\mathbf{u}_{n+1}\nabla_{\mathbf{X}}^T\mathbf{u}_{n+1}\right)\\=&\Delta t\nabla\cdot\mathbf{u}_{n+1}-\frac{\Delta t^2}{2}\left|\mathbf{F}_{n+1}^{-1}\nabla_{\mathbf{X}}\mathbf{u}_{n+1}\right|^2.\end{aligned}$$

In the above, we use the trace property of cyclic permutations: $tr\left(\mathbf{A_1}\mathbf{A_2}\mathbf{A_3}\right)=tr\left(\mathbf{A_2}\mathbf{A_3}\mathbf{A_1}\right)=tr\left(\mathbf{A_3}\mathbf{A_1}\mathbf{A_2}\right)$. □

From the above two lemmas, we have:

Proposition 8. *The energy function $\Psi(\mathbf{F})$ for the hyperelastic stress satisfies:*

$$\begin{aligned}&\int_{\Omega_{\mathbf{X}}^s} \Psi(\mathbf{F}_{n+1})\, d\mathbf{X} - \int_{\Omega_{\mathbf{X}}^s} \Psi(\mathbf{F}_n)\, d\mathbf{X} \\ &\leq \Delta t c_1 \int_{\Omega_{\mathbf{X}}^s} \mathbf{F}_{n+1} : \nabla_{\mathbf{X}} \mathbf{u}_{n+1} d\mathbf{X} - \Delta t c_1 \int_{\Omega_{n+1}^s} J_{n+1}^{-1} \nabla \cdot \mathbf{u}_{n+1} d\mathbf{x} + R_{n+1},\end{aligned} \tag{29}$$

where

$$R_{n+1} = \frac{c_1 \Delta t^2}{2} \int_{\Omega_{\mathbf{X}}^s} \left(\left| \mathbf{F}_{n+1}^{-1} \nabla_{\mathbf{X}} \mathbf{u}_{n+1} \right|^2 - \left| \nabla_{\mathbf{X}} \mathbf{u}_{n+1} \right|^2 \right) d\mathbf{X}. \tag{30}$$

Similarly to Lemma 4, we have:

Lemma 9. *If $(\mathbf{u}_{n+1}, p_{n+1})$ is the solution pair of Problem 2, then*

$$\int_{\Omega} (\mathbf{u}_{n+1} \cdot \nabla) \mathbf{u}_{n+1} \cdot \mathbf{u}_{n+1} d\mathbf{x} = 0. \tag{31}$$

Proposition 10 (Energy Stable)**.** *If $\rho^\delta \geq 0$, let $(\mathbf{u}_{n+1}, p_{n+1})$ be the solution pair of Problem 2, then*

$$\begin{aligned}&\frac{\rho^f}{2} \int_{\Omega} |\mathbf{u}_{n+1}|^2 d\mathbf{x} + \frac{\rho^\delta}{2} \int_{\Omega_{\mathbf{X}}^s} |\mathbf{u}_{n+1}|^2 d\mathbf{X} + \int_{\Omega_{\mathbf{X}}^s} \Psi(\mathbf{F}_{n+1})\, d\mathbf{X} \\ &+ \frac{\Delta t \mu^f}{2} \sum_{k=1}^{n+1} \int_{\Omega} \mathrm{D}\mathbf{u}_k : \mathrm{D}\mathbf{u}_k d\mathbf{x} + \frac{\Delta t \mu^\delta}{2} \sum_{k=1}^{n+1} \int_{\Omega_{n+1}^s} \mathrm{D}\mathbf{u}_k : \mathrm{D}\mathbf{u}_k d\mathbf{x} \\ &\leq \frac{\rho^f}{2} \int_{\Omega} |\mathbf{u}_n|^2 d\mathbf{x} + \frac{\rho^\delta}{2} \int_{\Omega_{\mathbf{X}}^s} |\mathbf{u}_n|^2 d\mathbf{X} + \int_{\Omega_{\mathbf{X}}^s} \Psi(\mathbf{F}_n)\, d\mathbf{X} \\ &+ \frac{\Delta t \mu^f}{2} \sum_{k=1}^{n} \int_{\Omega} \mathrm{D}\mathbf{u}_k : \mathrm{D}\mathbf{u}_k d\mathbf{x} + \frac{\Delta t \mu^\delta}{2} \sum_{k=1}^{n} \int_{\Omega_{n+1}^s} \mathrm{D}\mathbf{u}_k : \mathrm{D}\mathbf{u}_k d\mathbf{x} + R_{n+1},\end{aligned} \tag{32}$$

where R_{n+1} is defined in equation (30).

Proof. Let $\mathbf{v} = \mathbf{u}_{n+1}$ in (19) and multiply Δt on both side of the equation, and then let $q = p_{n+1}$ in (20) and substitute into equation (19), we get:

$$\begin{aligned}&\rho^f \int_{\Omega} (\mathbf{u}_{n+1} - \mathbf{u}_n) \cdot \mathbf{u}_{n+1} d\mathbf{x} + \frac{\Delta t \mu^f}{2} \int_{\Omega} \mathrm{D}\mathbf{u}_{n+1} : \mathrm{D}\mathbf{u}_{n+1} d\mathbf{x} \\ &+ \rho^\delta \int_{\Omega_{\mathbf{X}}^s} (\mathbf{u}_{n+1} - \mathbf{u}_n) \cdot \mathbf{u}_{n+1} d\mathbf{X} + \frac{\Delta t \mu^\delta}{2} \int_{\Omega_{n+1}^s} \mathrm{D}\mathbf{u}_{n+1} : \mathrm{D}\mathbf{u}_{n+1} d\mathbf{x} \\ &+ c_1 \Delta t \int_{\Omega_{\mathbf{X}}^s} \mathbf{F}_{n+1} : \nabla_{\mathbf{X}} \mathbf{u}_{n+1} d\mathbf{X} - c_1 \Delta t \int_{\Omega_{n+1}^s} \nabla \cdot \mathbf{u}_{n+1} d\mathbf{x} = 0.\end{aligned} \tag{33}$$

Using the Cauchy-Schwarz inequality and the fact $ab \leq \frac{a^2+b^2}{2}$, we have:

$$\int_{\omega} \mathbf{u}_n \cdot \mathbf{u}_{n+1} d\mathbf{x} \leq \|\mathbf{u}_n\|_{0,\omega} \|\mathbf{u}_{n+1}\|_{0,\omega} \leq \frac{\|\mathbf{u}_n\|_{0,\omega}^2 + \|\mathbf{u}_{n+1}\|_{0,\omega}^2}{2},$$

where $\omega = \Omega$ or Ω_{n+1}^s. Substituting the above relation into (33), we get (32) due to Proposition 8 and Lemma 9. □

Remark 3. *Relation (32) does not exactly show energy nonincreasing, because we do not know whether R_{n+1} is greater or less than 0. However, R_{n+1} is $O\left(\Delta t^2\right)$ and so in the worst possible case any growth in the energy is bounded by a term whose magnitude is smaller than the order of the error and which may be controlled easily and efficiently. Furthermore, it will be demonstrated through numerical tests in section 7 that this term has no identifiable impact for practical choices of time step. In order to test the energy property, let us use the following notation for the different contributions to the total energy in (32): (1) Kinetic energy of fluid plus fictitious fluid $E_k(\Omega) = \frac{\rho^f}{2} \int_{\Omega} |\mathbf{u}_n|^2 d\mathbf{x}$; (2) Kinetic energy of solid minus fictitious fluid $E_k(\Omega_{\mathbf{X}}^s) = \frac{\rho^\delta}{2} \int_{\Omega_{\mathbf{X}}^s} |\mathbf{u}_n|^2 d\mathbf{X}$; (3) Viscous dissipation $E_d(\Omega) = \frac{\Delta t \mu^f}{2} \sum_{k=0}^{n} \int_{\Omega} \mathrm{D}\mathbf{u}_k : \mathrm{D}\mathbf{u}_k d\mathbf{x} + \frac{\Delta t \mu^\delta}{2} \sum_{k=0}^{n} \int_{\Omega_{n+1}^s} \mathrm{D}\mathbf{u}_k : \mathrm{D}\mathbf{u}_k d\mathbf{x}$; (4) Potential energy of the solid $E_p(\Omega_{\mathbf{X}}^s) = \int_{\Omega_{\mathbf{X}}^s} \Psi(\mathbf{F}_n) d\mathbf{X}$. Denote the total energy at as $E_{total} = E_k(\Omega) + E_k(\Omega_{\mathbf{X}}^s) + E_d(\Omega) + E_p(\Omega_{\mathbf{X}}^s)$, and the energy ratio as:*

$$E_{ratio} = \frac{E_{total}(t_n)}{E_{total}(t_0)}. \tag{34}$$

We shall numerically demonstrate that E_{ratio} is nonincreasing in section 7.

6. Discretization in space

We shall use a fixed Eulerian mesh for Ω and an updated Lagrangian mesh for Ω_{n+1}^s to discretize Problem 2. First, we discretize Ω as Ω^h with the corresponding finite element spaces as

$$V^h(\Omega^h) = span\left\{\varphi_1, \cdots, \varphi_{N^u}\right\} \subset H_0^1(\Omega)$$

and

$$L^h(\Omega^h) = span\left\{\phi_1, \cdots, \phi_{N^p}\right\} \subset L_0^2(\Omega).$$

The approximated solution $\mathbf{u}^h$ and p^h can be expressed in terms of these basis functions as

$$\mathbf{u}^h(\mathbf{x}) = \sum_{i=1}^{N^u} \mathbf{u}(\mathbf{x}_i)\varphi_i(\mathbf{x}), \quad p^h(\mathbf{x}) = \sum_{i=1}^{N^p} p(\mathbf{x}_i)\phi_i(\mathbf{x}). \tag{35}$$

We further discretize Ω_0^s as Ω_0^{sh} with the corresponding finite element spaces as:

$$V^{sh}(\Omega_0^{sh}) = span\left\{\varphi_1^s, \cdots, \varphi_{N^s}^s\right\} \subset H^1(\Omega_0^s),$$

then move the vertices of each element of Ω_n^{sh} by their own velocities to get Ω_{n+1}^{sh}, and approximate $\mathbf{u}^h(\mathbf{x})\big|_{\mathbf{x}\in\Omega_{n+1}^{sh}}$ as:

$$\mathbf{u}^{sh}(\mathbf{x}) = \sum_{i=1}^{N^s} \mathbf{u}^h(\mathbf{x}_i^s)\varphi_i^s(\mathbf{x}) = \sum_{i=1}^{N^s}\sum_{j=1}^{N^u} \mathbf{u}(\mathbf{x}_j)\varphi_j(\mathbf{x}_i^s)\varphi_i^s(\mathbf{x}), \tag{36}$$

where $\mathbf{x}_i^s$ is the nodal coordinate of the solid mesh. Notice that the above approximation defines an L^2 projection P_{n+1} from $V^h\left(\Omega^h\right)^d$ to $V^{sh}\left(\Omega_{n+1}^{sh}\right)^d$: $P_{n+1}\left(\mathbf{u}^h(\mathbf{x})\right) = \mathbf{u}^{sh}(\mathbf{x})$,

We then discretize Problem 2 in space as follows.

Problem 11. *Given $\mathbf{u}_n^h$, p_n^h and Ω_n^{sh}, find $\mathbf{u}_{n+1}^h \in V^h(\Omega^h)^d$, $p_{n+1}^h \in L^h(\Omega^h)$ and Ω_{n+1}^{sh}, such that for $\forall \mathbf{v} \in V^h(\Omega^h)^d$, $\forall q \in L^h(\Omega^h)$, the following four relations hold:*

$$\begin{aligned}
&\rho^f \int_{\Omega^h} \frac{\mathbf{u}_{n+1}^h - \mathbf{u}_n^h}{\Delta t}\cdot\mathbf{v}d\mathbf{x} + \rho^f \int_{\Omega^h} \left(\mathbf{u}_{n+1}^h\cdot\nabla\right)\mathbf{u}_{n+1}^h\cdot\mathbf{v}d\mathbf{x} \\
&+ \frac{\mu^f}{2}\int_{\Omega^h} \mathrm{D}\mathbf{u}_{n+1}^h : \mathrm{D}\mathbf{v}d\mathbf{x} - \int_{\Omega^h} p_{n+1}^h \nabla\cdot\mathbf{v}d\mathbf{x} \\
&+ \rho^\delta \int_{\Omega_{\mathbf{X}}^{sh}} \frac{\mathbf{u}_{n+1}^{sh} - \mathbf{u}_n^{sh}}{\Delta t}\cdot\mathbf{v}^s d\mathbf{X} + \frac{\mu^\delta}{2}\int_{\Omega_{n+1}^{sh}} \mathrm{D}\mathbf{u}_{n+1}^h : \mathrm{D}\mathbf{v}d\mathbf{x} \\
&+ c_1\Delta t \int_{\Omega_{\mathbf{X}}^{sh}} \nabla_{\mathbf{X}}\mathbf{u}_{n+1}^{sh} : \nabla_{\mathbf{X}}\mathbf{v}^s d\mathbf{X} \\
&- c_1 \int_{\Omega_{n+1}^{sh}} J_{n+1}^{-1}\nabla\cdot\mathbf{v}^s d\mathbf{x} = -c_1\int_{\Omega_{\mathbf{X}}^{sh}} \mathbf{F}_n^{sh} : \nabla_{\mathbf{X}}\mathbf{v}^s d\mathbf{X},
\end{aligned} \tag{37}$$

$$-\int_\Omega q\nabla\cdot\mathbf{u}_{n+1}^h d\mathbf{x} = 0, \tag{38}$$

$$\Omega_{n+1}^{sh} = \left\{\mathbf{x} : \mathbf{x} = \mathbf{x}_n + \Delta t\mathbf{u}_{n+1}^{sh}, \mathbf{x}_n \in \Omega_n^{sh}\right\}, \tag{39}$$

and

$$\mathbf{F}_{n+1}^{sh} = \mathbf{F}_n^{sh} + \Delta t\nabla_{\mathbf{X}}\mathbf{u}_{n+1}^{sh}, \tag{40}$$

where $\mathbf{u}^{sh} = P_{n+1}\left(\mathbf{u}^h\right)$ and $\mathbf{v}^s = P_{n+1}(\mathbf{v})$.

Remark 4. *The proof of the energy estimate (Proposition 10) for the spatially continuous case can also be applied to the discrete case (see Appendix A).*

Remark 5. *There are two sources of nonlinearity in Problem 11: the convection term and the moving solid domain. We can accommodate these by moving the convection term to the right-hand side of the equation, and using a fixed-point iteration to construct Ω_{n+1}^s in order to solve the nonlinear system at each time step. For other methods to treat convection, readers may refer to [26, 27]. We shall only use this fully implicit implementation to consider low Reynolds number cases in this paper in order to test the energy stability.*

Remark 6. *A two-step explicit splitting scheme (**F**-scheme) is discussed in Appendix B with corresponding energy analysis. This scheme is similar to that in [1] ($\boldsymbol{\sigma}$-scheme), which may be adapted to problems at large Reynolds number (see [1] for more examples).*

7. Numerical experiments

In this section, we focus on validation of the energy stability of the proposed numerical method in two and three dimensions. For more two-dimensional numerical examples and validation of the basic algorithm see [1]. We shall use linear triangles (2D) or linear tetrahedra (3D) to discretize the solid domain Ω_0^s. In domain Ω, the $P_2/(P_1 + P_0)$ elements will be used, i.e., the standard *Taylor-Hood* element P_2P_1 is enriched by a constant P_0 for approximation of the pressure. This element has the property of local mass conservation and the constant P_0 may better capture the element-based jump of pressure [28, 29]. We shall demonstrate the improvement of mass conservation and energy conservation by using the $P_2/(P_1 + P_0)$ elements compared to the P_2P_1 elements. We shall also validate that the total energy is nonincreasing as stated in Proposition 10 and Remark 3.

7.1. Oscillating disc driven by an initial kinetic energy (activated disc)

In this test, we consider an enclosed flow ($\mathbf{n} \cdot \mathbf{u} = 0$) in $\Omega = [0, 1] \times [0, 1]$ with a periodic boundary condition. A solid disc is initially located in the middle of the square Ω and has a radius of 0.2. The initial velocity of the fluid and solid are prescribed by the following stream function

$$\Psi = \Psi_0 \sin(ax)\sin(by),$$

where $\Psi_0 = 5.0 \times 10^{-2}$ and $a = b = 2\pi$. In this test, $\rho^f = 1$, $\mu^s = \mu^f = 0.01$, $\rho^s = 1.5$ and $c_1 = 1$. In order to visualize the flow a snapshot of the velocity and deformation fields is presented in Figure 2, and the evolution of energy is presented in Figure 3 using a 50×50 mesh (biquadratic squares for the fluid velocity and 3052 bilinear triangles for the solid velocity).

We commence by comparing P_2/P_1 elements and $P_2/(P_1 + P_0)$ elements. The evolution of mass variation and energy ratio are demonstrated in Figure 4, from which it can be seen that the enrichment of the pressure field by a constant P_0 has an effect of stabilizing the mass and energy evolution. In addition, this enrichment of the pressure field dramatically improves the mass conservation, although the effect for energy conservation appears to be negative. Then using element $P_2/(P_1 + P_0)$, time convergence of the total energy can be observed from Figure 5 (a), from which we can see a nonincreasing energy and a first order time convergence for both the implicit and explicit scheme (see Appendix B for the energy estimate of the explicit scheme). It can be seen from Figure 5 (b) that the residual term defined in (30) is very small and converges rapidly to zero when reducing Δt ($\sim O(\Delta t^2)$).

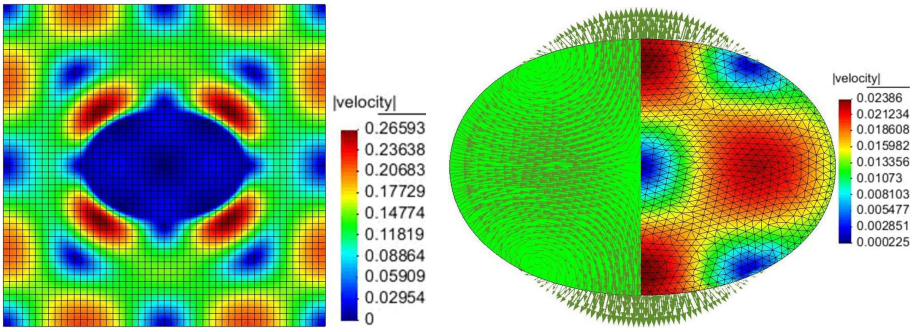

(a) Velocity norm on the fluid mesh, (b) Distribution of velocity on the solid mesh.

Figure 2: Snapshot at $t = 0.25$, $\Delta t = 5.0 \times 10^{-3}$.

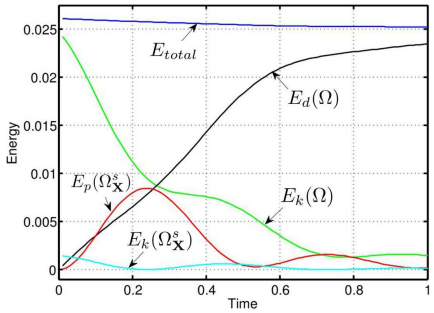

Figure 3: Evolution of energy, $\Delta t = 5.0 \times 10^{-3}$.

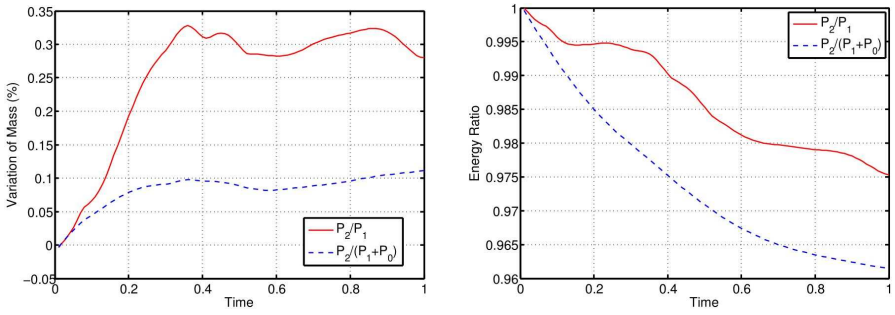

(a) Variation of mass against time, (b) Energy ratio (see (34)) against time.

Figure 4: Variation of mass and energy, $\Delta t = 5.0 \times 10^{-3}$.

7.2. Oscillating disc driven by an initial potential energy (stretched disc)

In the previous example, the disc oscillates because a kinetic energy is prescribed for the FSI system at the beginning. In this test, we shall stretch the disc and create a potential energy in the solid, then release it causing the disc to oscillate due to this potential energy. The computational domain is a square

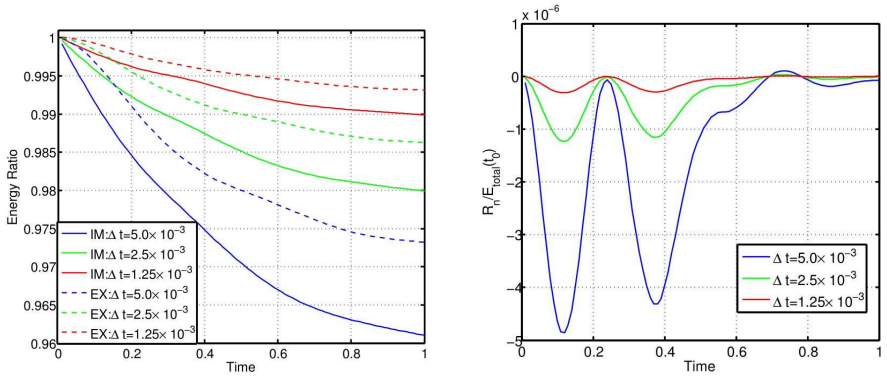

(a) Energy ratio against time (defined in (34)), (b) $R_n/E_{total}\,(t_0)$ against time (defined in (30)).

Figure 5: Evolution of the energy ratio and residual R_n for the test problem of activated disc.

$\Omega = [0,1]\times[0,1]$. One quarter of a solid disc is located in the left-bottom corner of the square, and initially stretched as an ellipse as shown in Figure 6. Notice the equation of an ellipse $\frac{x^2}{a^2}+\frac{y^2}{b^2}=1$ and its area πab, hence we ensure that this stretch does not change mass of the solid.

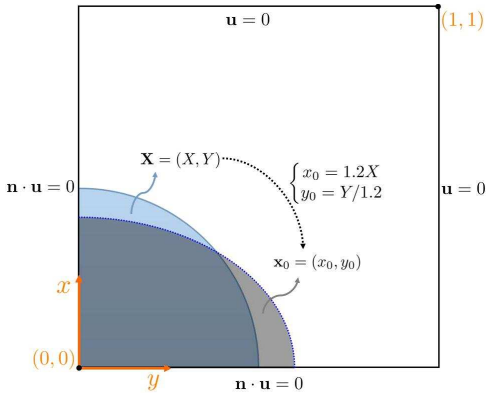

Figure 6: Computational domain and boundary conditions for test problem 7.2 (stretched disc).

We choose $\rho^f = 1$, $\mu^s = \mu^f = 0.01$, $\rho^s = 2$ and $c_1 = 2$. The fluid adopts a mesh of 66×66 biquadratic squares, and the solid has similar node density (8206 linear triangles) as the fluid. A snapshot of pressure on the fluid mesh and corresponding solid deformation with its velocity norm are displayed in Figure 7, and the evolution of energy is presented in Figure 8. The nonincreasing total energy can be observed from Figure 9 (a) for both the implicit and explicit scheme (see Appendix B for energy estimate of the explicit scheme). It can be seen from Figure 9 (b) that the residual term defined in (30) is very small and converges rapidly to zero when reducing Δt.

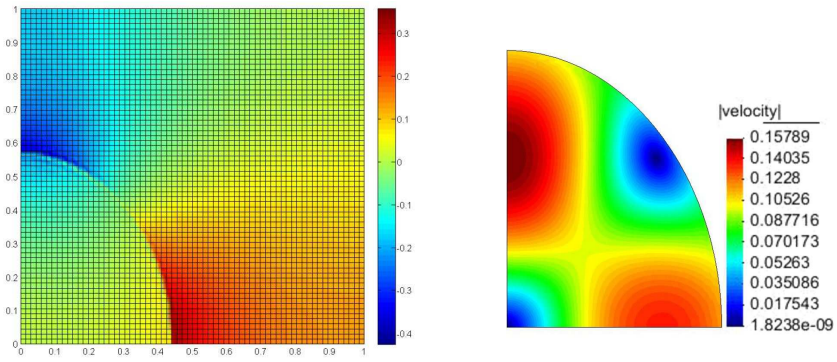

(a) Distribution of pressures on the fluid mesh, (b) velocity norm on the solid.

Figure 7: A snapshot at $t = 1$, $\Delta t = 5.0 \times 10^{-3}$.

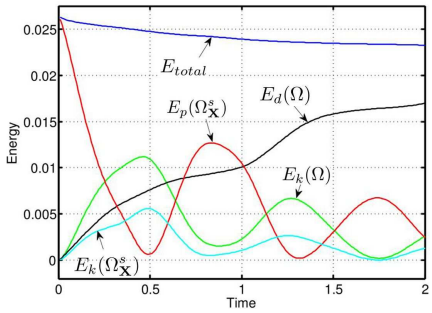

Figure 8: Evolution of energy, $\Delta t = 5.0 \times 10^{-3}$.

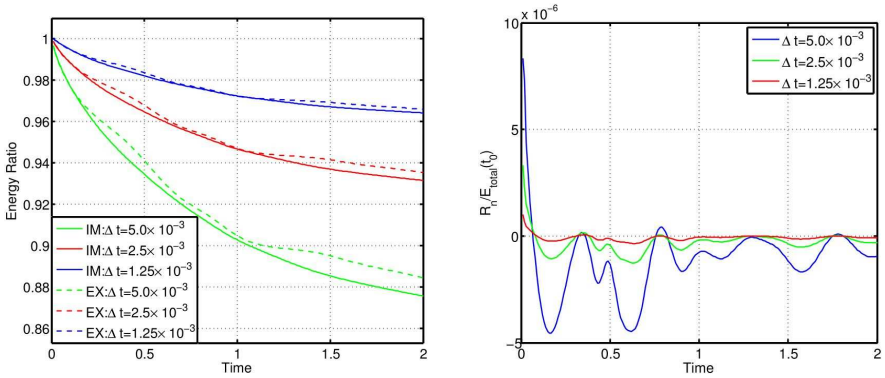

(a) Energy ratio against time (defined in (34)), (b) $R_n/E_{total}\,(t_0)$ against time (defined in (30)).

Figure 9: Evolution of the energy ratio and residual R_n for the test problem of stretched disc.

7.3. Rotating cross driven by an initial kinetic energy (rotating cross)

In this test, we consider an enclosed flow in $\Omega = [-0.5, 0.5] \times [-0.5, 0.5]$ with a slip boundary condition ($\mathbf{n} \cdot \mathbf{u} = 0$). A solid cross, made up of two 0.1×0.5 rectangles as shown in Figure 10 (a), is initially located in the middle of the square domain Ω, with the centre pinned at the origin for all time. A rotating velocity field is initially prescribed to the fluid and solid as follows:

$$\mathbf{u} = U\boldsymbol{\tau}, \quad U = 4r(r_0 - r)/r_0^2, \quad r = \sqrt{x^2 + y^2}, \quad \boldsymbol{\tau} = (-y, x)/r, \tag{41}$$

where $r_0 = 0.5$ and $(x, y) \in \Omega$.

We use the same fluid properties as used in the activated disc (section 7.1). In addition, we also use the same solid properties but extend the parameter c_1 to three different cases: $c_1 = 1$, 10 and 100, in order to investigate the response of the FSI system according to the solid stiffness. We use 50×50 $P_2/(P_1 + P_0)$ elements to discretize the background fluid domain, and 3600 structured linear triangles (see Figure 10) to discretize the solid cross. A small time step of $\Delta t = 5.0 \times 10^{-4}$ is used for all the three cases, and the deformed solids are presented in Figure 10. It can be seen from these figures that the solid already behaves like a rigid body when $c_1 = 100$. The evolution of the total energy is also presented in Figure 12, from which it can be seen that the total energy is non-increasing for the three different solid cases.

7.4. Oscillating ball driven by an initial kinetic energy

In this section, we consider a 3D oscillating ball, which is an extension of the example in section 7.1. The ball is initially located at the center of $\Omega = [0, 1] \times [0, 1] \times [0, 0.6]$ with a radius of 0.2. Using the property of symmetry this computation is carried out on 1/8 of domain Ω: $[0, 0.5] \times [0, 0.5] \times [0, 0.3]$. The initial velocities of x and y components are the same as that used in section 7.1 and the z component is set to be 0 at the beginning. We adopt the same parameter and mesh size defined in section 7.1 (with the same mesh size in the z direction). A snapshot of the 1/8 solid ball and the corresponding fluid velocity norm are presented in Figure 13, and the nonincreasing energy property is presented in Figure 14.

8. Conclusions

In this article, we first introduce an implicit version of [1] for the one-field fictitious domain method (one-field FDM) based upon updating the solid deformation tensor $\mathbf{F}$. Then the energy-preserving property for this one-field FDM is proved on the continuous level, and the energy-stability property is proved after discretization in time and space. The energy property for an explicit scheme is also analyzed in Appendix B. Finally, a selection of numerical tests are presented to demonstrate this theoretical energy estimate in both two and three dimensions.

Whilst the purpose of this paper is to analyse the stability of the computational scheme introduced in [1], we also briefly comment on the computational

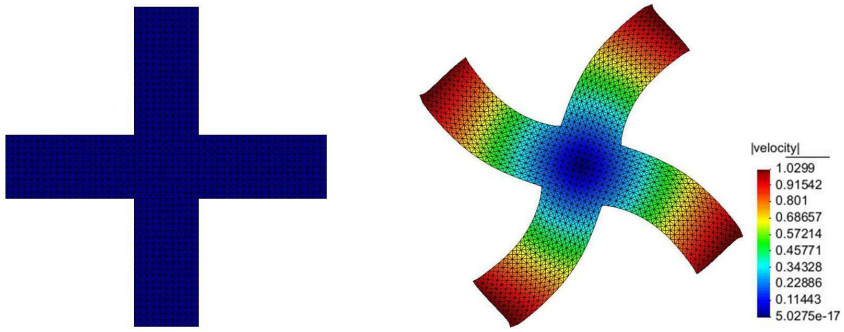

(a) Initial configuration.

(b) $c_1 = 1$ at $t = 0.28$.

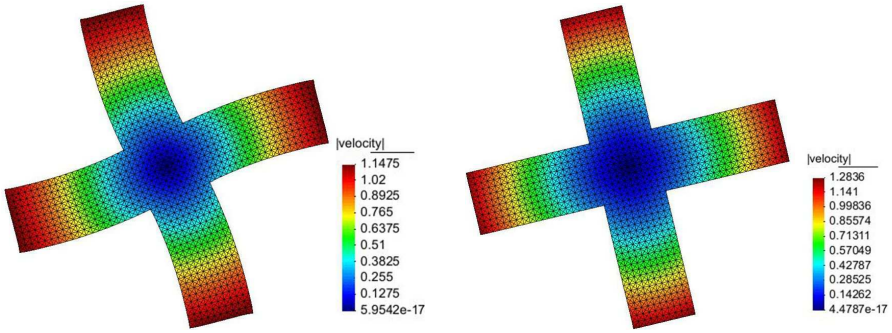

(c) $c_1 = 10$ at $t = 0.08$.

(d) $c_1 = 100$ at $t = 0.05$.

Figure 10: Solid crosses displayed when they are maximally deformed according to the potential energy shown in Figure 11.

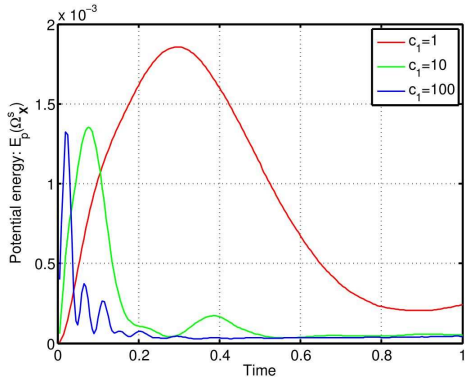

Figure 11: Potential energy for three different stiffnesses of the solid.

efficiency relative to the immersed finite element method. For those problems where the IFEM scheme works best (e.g. soft viscoelastic solids with identical viscosity to the surrounding fluid) we find our implementation of the one-field FD method is only marginally slower (no more than 1% in the experiments that

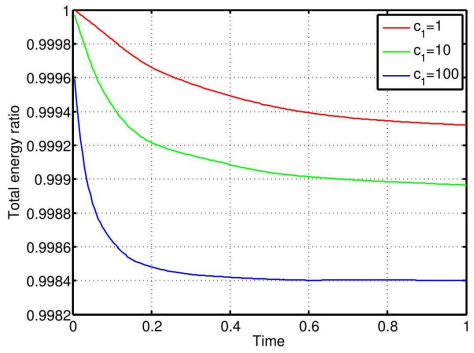

Figure 12: Evolution of the energy ratio (defined in (34)) for the test problem of rotating cross.

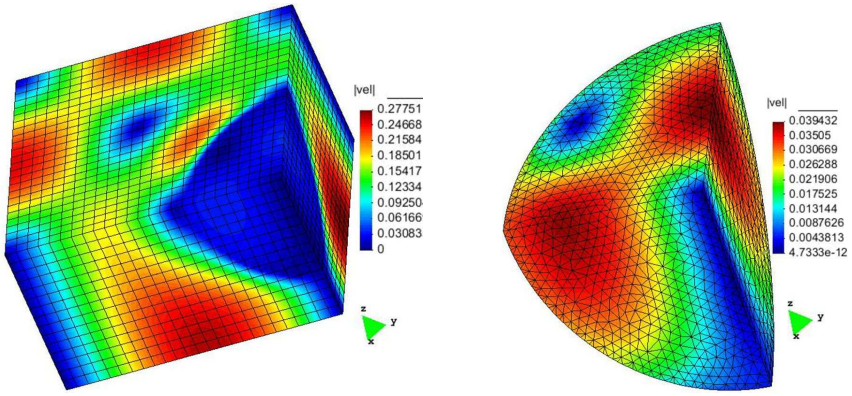

(a) Fluid mesh, (b) solid mesh.

Figure 13: Velocity norm at $t = 0.2$.

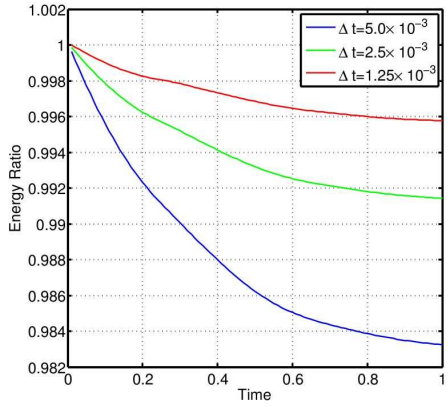

Figure 14: Evolution of the energy ratio (defined in (34)) for the test problem of oscillating ball.

we have undertaken). However, we find that the one-field FDM is far more robust that the IFEM, which means that for most problems it is able to solve in a significantly shorter computational time: including cases where the IFEM is unable to converge.

Appendix A. Stability analysis after space discretization

As with the previous stability estimate (Proposition 10) after time discretization, we have the following estimate after space discretization.

Proposition 12. *If $\rho^\delta \geq 0$, let $\left(\mathbf{u}_{n+1}^h, p_{n+1}^h\right)$ be the solution pair of Problem 11, then*

$$\begin{aligned}
&\frac{\rho^f}{2}\int_{\Omega^h}\left|\mathbf{u}_{n+1}^h\right|^2 d\mathbf{x} + \frac{\rho^\delta}{2}\int_{\Omega_{\mathbf{X}}^{sh}}\left|\mathbf{u}_{n+1}^{sh}\right|^2 d\mathbf{X} + \int_{\Omega_{\mathbf{X}}^{sh}}\Psi\left(\mathbf{F}_{n+1}^{sh}\right)d\mathbf{X} \\
&+ \frac{\Delta t\mu^f}{2}\sum_{k=1}^{n+1}\int_{\Omega^h}\mathrm{D}\mathbf{u}_k^h : \mathrm{D}\mathbf{u}_k^h d\mathbf{x} + \frac{\Delta t\mu^\delta}{2}\sum_{k=1}^{n+1}\int_{\Omega_{n+1}^{sh}}\mathrm{D}\mathbf{u}_k^{sh} : \mathrm{D}\mathbf{u}_k^{sh} d\mathbf{x} \\
&\leq \frac{\rho^f}{2}\int_{\Omega^h}\left|\mathbf{u}_n^h\right|^2 d\mathbf{x} + \frac{\rho^\delta}{2}\int_{\Omega_{\mathbf{X}}^{sh}}\left|\mathbf{u}_n^{sh}\right|^2 d\mathbf{X} + \int_{\Omega_{\mathbf{X}}^{sh}}\Psi\left(\mathbf{F}_n^{sh}\right)d\mathbf{X} \\
&+ \frac{\Delta t\mu^f}{2}\sum_{k=1}^{n}\int_{\Omega^h}\mathrm{D}\mathbf{u}_k^h : \mathrm{D}\mathbf{u}_k^h d\mathbf{x} + \frac{\Delta t\mu^\delta}{2}\sum_{k=1}^{n}\int_{\Omega_{n+1}^{sh}}\mathrm{D}\mathbf{u}_k^{sh} : \mathrm{D}\mathbf{u}_k^{sh} d\mathbf{x} + R_{n+1}^h,
\end{aligned} \tag{A.1}$$

where

$$R_{n+1}^h = \frac{c_1\Delta t^2}{2}\int_{\Omega_{\mathbf{X}}^{sh}}\left(\left|\left(\mathbf{F}_{n+1}^{sh}\right)^{-1}\nabla_{\mathbf{X}}\mathbf{u}_{n+1}^{sh}\right|^2 - \left|\nabla_{\mathbf{X}}\mathbf{u}_{n+1}^{sh}\right|^2\right)d\mathbf{X}. \tag{A.2}$$

Proof. Let $\mathbf{v} = \mathbf{u}_{n+1}^h$ in (37) and multiply Δt on both side of the equation, and then let $q = p_{n+1}^h$ in (38) and substitute into equation (37), we get:

$$\begin{aligned}
&\rho^f\int_{\Omega^h}\left(\mathbf{u}_{n+1}^h - \mathbf{u}_n^h\right)\cdot\mathbf{u}_{n+1}^h d\mathbf{x} + \frac{\Delta t\mu^f}{2}\int_{\Omega^h}\mathrm{D}\mathbf{u}_{n+1}^h : \mathrm{D}\mathbf{u}_{n+1}^h d\mathbf{x} \\
&+ \rho^\delta\int_{\Omega_{\mathbf{X}}^{sh}}\left(\mathbf{u}_{n+1}^{sh} - \mathbf{u}_n^{sh}\right)\cdot\mathbf{u}_{n+1}^{sh} d\mathbf{X} + \frac{\Delta t\mu^\delta}{2}\int_{\Omega_{n+1}^{sh}}\mathrm{D}\mathbf{u}_{n+1}^h : \mathrm{D}\mathbf{u}_{n+1}^h d\mathbf{x} \\
&+ c_1\Delta t\int_{\Omega_{\mathbf{X}}^{sh}}\mathbf{F}_{n+1}^{sh} : \nabla_{\mathbf{X}}\mathbf{u}_{n+1}^{sh} d\mathbf{X} - c_1\Delta t\int_{\Omega_{n+1}^{sh}}\nabla\cdot\mathbf{u}_{n+1}^{sh} d\mathbf{x} = 0.
\end{aligned} \tag{A.3}$$

Using the Cauchy-Schwarz inequality and the fact $ab \leq \frac{a^2+b^2}{2}$, we have:

$$\int_\omega \mathbf{u}_n\cdot\mathbf{u}_{n+1} d\mathbf{x} \leq \|\mathbf{u}_n\|_{0,\omega}\|\mathbf{u}_{n+1}\|_{0,\omega} \leq \frac{\|\mathbf{u}_n\|_{0,\omega}^2 + \|\mathbf{u}_{n+1}\|_{0,\omega}^2}{2},$$

where $\omega = \Omega^h$ or Ω_{n+1}^{sh}. Notice that Lemma 6 to 9 still hold after space discretization, then substituting the above relation into (A.3) gives (A.1). □

Remark 7. *In relation (A.1), the velocity* $\mathbf{u}^{sh} = P_{n+1}\left(\mathbf{u}^h\right)$ *(after interpolation) is used to evaluate (or define) the energy terms for the solid. Therefore the interpolation error itself does not appear in the estimate relation (A.1). The energy estimate of Proposition 12 is an indication of solution stability and existence of Problem 11, which requires iterations in order to construct the current domain* Ω_{n+1}^{sh} *and build the interpolation function* P_{n+1}*. If the iterations can be proved to converge (interpolation error appears here), then the solution existence for Problem 11 is proved. At the moment we have estimated the energy as demonstrated in Proposition 12, the solution existence may be proved based on this energy estimate in our future work.*

Appendix B. Energy estimate for a two-step explicit splitting scheme

In this section, we analyze the energy property for the 2-step explicit splitting scheme introduced in [1], which can be stated as follows (corresponding to the implicit Problem 11):

Problem 13. *Given* $\mathbf{u}_n^h$*,* p_n^h *and* Ω_n^{sh}*, find* $\mathbf{u}_{n+1}^h \in V^h(\Omega^h)^d$*,* $p_{n+1}^h \in L^h(\Omega^h)$ *and* Ω_{n+1}^{sh}*, such that for* $\forall \mathbf{v} \in V^h(\Omega^h)^d$*,* $\forall q \in L^h(\Omega^h)$*, the following 5 relations hold:*

(1) convetion step:

$$\rho^f \int_{\Omega^h} \frac{\mathbf{u}_{n+1/2}^h - \mathbf{u}_n^h}{\Delta t} \cdot \mathbf{v} d\mathbf{x} + \rho^f \int_{\Omega^h} \left(\mathbf{u}_{n+1/2}^h \cdot \nabla\right) \mathbf{u}_{n+1/2}^h \cdot \mathbf{v} d\mathbf{x} = 0, \tag{B.1}$$

(2) diffusion step:

$$\begin{aligned}
&\rho^f \int_{\Omega^h} \frac{\mathbf{u}_{n+1}^h - \mathbf{u}_{n+1/2}^h}{\Delta t} \cdot \mathbf{v} d\mathbf{x} + \frac{\mu^f}{2} \int_{\Omega^h} \mathrm{D}\mathbf{u}_{n+1}^h : \mathrm{D}\mathbf{v} d\mathbf{x} \\
&- \int_{\Omega^h} p_{n+1}^h \nabla \cdot \mathbf{v} d\mathbf{x} + \rho^\delta \int_{\Omega_{\mathbf{X}}^{sh}} \frac{\mathbf{u}_{n+1}^{sh} - \mathbf{u}_n^{sh}}{\Delta t} \cdot \mathbf{v}^s d\mathbf{X} \\
&+ c_1 \Delta t \int_{\Omega_{\mathbf{X}}^{sh}} \nabla_{\mathbf{X}} \mathbf{u}_{n+1}^{sh} : \nabla_{\mathbf{X}} \mathbf{v}^s d\mathbf{X} + \frac{\mu^\delta}{2} \int_{\Omega_{n+1}^{sh}} \mathrm{D}\mathbf{u}_{n+1}^h : \mathrm{D}\mathbf{v} d\mathbf{x} \\
&- c_1 \int_{\Omega_n^{sh}} J_n^{-1} \nabla_n \cdot \mathbf{v}^s d\mathbf{x} = -c_1 \int_{\Omega_{\mathbf{X}}^{sh}} \mathbf{F}_n^{sh} : \nabla_{\mathbf{X}} \mathbf{v}^s d\mathbf{X},
\end{aligned} \tag{B.2}$$

$$-\int_{\Omega} q \nabla \cdot \mathbf{u}_{n+1}^h d\mathbf{x} = 0, \tag{B.3}$$

$$\Omega_{n+1}^{sh} = \left\{\mathbf{x} : \mathbf{x} = \mathbf{x}_n + \Delta t \mathbf{u}_{n+1}^{sh}, \mathbf{x}_n \in \Omega_n^{sh}\right\}, \tag{B.4}$$

and

$$\mathbf{F}_{n+1}^{sh} = \mathbf{F}_n^{sh} + \Delta t \nabla_{\mathbf{X}} \mathbf{u}_{n+1}^{sh}, \tag{B.5}$$

where $\mathbf{u}^{sh} = P_{n+1}\left(\mathbf{u}^h\right)$*,* $\mathbf{v}^s = P_{n+1}\left(\mathbf{v}\right)$*, and* $\nabla_n(\cdot) = \frac{\partial(\cdot)}{\partial \mathbf{x}_n}$*.*

As with the previous analysis for the implicit scheme, if we let $\mathbf{v} = \mathbf{u}^h_{n+1}$ in equations (B.1), (B.2) and (B.3), adding up these three equations, using (B.5) and $\mathbf{u}^{sh} = P_{n+1}\left(\mathbf{u}^h\right)$, gives the energy estimate as follows.

Proposition 14. *If $\rho^\delta \geq 0$, let $(\mathbf{u}_{n+1}, p_{n+1})$ be the solution pair of Problem 13, then*

$$\begin{aligned}
&\frac{\rho^f}{2}\int_{\Omega^h}\left|\mathbf{u}^h_{n+1}\right|^2 d\mathbf{x} + \frac{\rho^\delta}{2}\int_{\Omega^{sh}_{\mathbf{X}}}\left|\mathbf{u}^h_{n+1}\right|^2 d\mathbf{X} + \int_{\Omega^{sh}_{\mathbf{X}}}\Psi\left(\mathbf{F}^{sh}_{n+1}\right) d\mathbf{X} \\
&+ \frac{\Delta t\mu^f}{2}\sum_{k=1}^{n+1}\int_{\Omega^h} \mathrm{D}\mathbf{u}^h_k : \mathrm{D}\mathbf{u}^h_k d\mathbf{x} \\
&\leq \frac{\rho^f}{2}\int_{\Omega^h}\left|\mathbf{u}^h_n\right|^2 d\mathbf{x} + \frac{\rho^\delta}{2}\int_{\Omega^{sh}_{\mathbf{X}}}\left|\mathbf{u}^h_n\right|^2 d\mathbf{X} + \int_{\Omega^{sh}_{\mathbf{X}}}\Psi\left(\mathbf{F}^{sh}_n\right) d\mathbf{X} \\
&+ \frac{\Delta t\mu^f}{2}\sum_{k=1}^{n}\int_{\Omega^h} \mathrm{D}\mathbf{u}^h_k : \mathrm{D}\mathbf{u}^h_k d\mathbf{x} + R^{im}_{n+1} + R^{ex}_{n+1} + R^{split}_{n+1},
\end{aligned} \tag{B.6}$$

where $R^{im}_{n+1} = R^h_{n+1}$ as defined in (A.2).

$$R^{ex}_{n+1} = c_1\Delta t\int_{\Omega^{sh}_{\mathbf{X}}}\left(\nabla_n\cdot\mathbf{u}^{sh}_{n+1} - \nabla\cdot\mathbf{u}^{sh}_{n+1}\right) d\mathbf{X}, \tag{B.7}$$

and

$$R^{split}_{n+1} = \Delta t\rho^f\int_{\Omega^h}\left(\mathbf{u}^h_{n+1/2}\cdot\nabla\right)\mathbf{u}^h_{n+1/2}\cdot\mathbf{u}^h_{n+1} d\mathbf{x}. \tag{B.8}$$

References

[1] Y. Wang, P. K. Jimack, M. A. Walkley, A one-field monolithic fictitious domain method for fluid–structure interactions, Computer Methods in Applied Mechanics and Engineering 317 (2017) 1146–1168. doi:10.1016/j.cma.2017.01.023.

[2] X. Wang, C. Wang, L. T. Zhang, Semi-implicit formulation of the immersed finite element method, Computational Mechanics 49 (4) (2011) 421–430. doi:10.1007/s00466-011-0652-z.

[3] X. Wang, L. T. Zhang, Interpolation functions in the immersed boundary and finite element methods, Computational Mechanics 45 (4) (2009) 321–334. doi:10.1007/s00466-009-0449-5.

[4] X. Wang, L. T. Zhang, Modified immersed finite element method for fully-coupled fluid–structure interactions, Computer Methods in Applied Mechanics and Engineering 267 (2013) 150–169. doi:10.1016/j.cma.2013.07.019.

[5] L. Zhang, M. Gay, Immersed finite element method for fluid-structure interactions, Journal of Fluids and Structures 23 (6) (2007) 839–857. doi:10.1016/j.jfluidstructs.2007.01.001.

[6] L. Zhang, A. Gerstenberger, X. Wang, W. K. Liu, Immersed finite element method, Computer Methods in Applied Mechanics and Engineering 193 (21) (2004) 2051–2067. doi:doi:10.1016/j.cma.2003.12.044.

[7] F. P. Baaijens, A fictitious domain/mortar element method for fluid-structure interaction, International Journal for Numerical Methods in Fluids 35 (7) (2001) 743–761. doi:10.1002/1097-0363(20010415)35:7<743::AID-FLD109>3.0.CO;2-A.

[8] D. Boffi, L. Gastaldi, A fictitious domain approach with Lagrange multiplier for fluid-structure interactions, Numerische Mathematik 135 (3) (2016) 711–732. doi:10.1007/s00211-016-0814-1.

[9] R. Glowinski, T. Pan, T. Hesla, D. Joseph, J. Périaux, A fictitious domain approach to the direct numerical simulation of incompressible viscous flow past moving rigid bodies: Application to particulate flow, Journal of Computational Physics 169 (2) (2001) 363–426. doi:10.1006/jcph.2000.6542.

[10] C. Hesch, A. Gil, A. A. Carreño, J. Bonet, P. Betsch, A mortar approach for fluid–structure interaction problems: Immersed strategies for deformable and rigid bodies, Computer Methods in Applied Mechanics and Engineering 278 (2014) 853–882. doi:10.1016/j.cma.2014.06.004.

[11] C. Kadapa, W. Dettmer, D. Perić, A fictitious domain/distributed Lagrange multiplier based fluid–structure interaction scheme with hierarchical b-spline grids, Computer Methods in Applied Mechanics and Engineering 301 (2016) 1–27. doi:10.1016/j.cma.2015.12.023.

[12] Z. Yu, A DLM/FD method for fluid/flexible-body interactions, Journal of Computational Physics 207 (1) (2005) 1–27. doi:10.1016/j.jcp.2004.12.026.

[13] F. Hecht, O. Pironneau, An energy stable monolithic Eulerian fluid-structure finite element method, International Journal for Numerical Methods in Fluidsdoi:10.1002/fld.4388.

[14] O. Pironneau, Numerical study of a monolithic fluid–structure formulation, in: Variational Analysis and Aerospace Engineering, Springer International Publishing, 2016, pp. 401–420. doi:10.1007/978-3-319-45680-5_15.
URL https://doi.org/10.1007%2F978-3-319-45680-5_15

[15] A. Legay, J. Chessa, T. Belytschko, An Eulerian–Lagrangian method for fluid–structure interaction based on level sets, Computer Methods in Applied Mechanics and Engineering 195 (17) (2006) 2070–2087.

[16] T. Dunne, R. Rannacher, Adaptive finite element approximation of fluid-structure interaction based on an Eulerian variational formulation, in: Lecture Notes in Computational Science and Engineering, Springer Science Business Media, 2006, pp. 110–145. doi:10.1007/3-540-34596-5_6.

[17] T. Richter, T. Wick, Finite elements for fluid–structure interaction in ALE and fully Eulerian coordinates, Computer Methods in Applied Mechanics and Engineering 199 (41-44) (2010) 2633–2642. doi:10.1016/j.cma.2010.04.016.
URL https://doi.org/10.1016%2Fj.cma.2010.04.016

[18] T. Richter, A fully Eulerian formulation for fluid–structure-interaction problems, Journal of Computational Physics 233 (2013) 227–240. doi:10.1016/j.jcp.2012.08.047.

[19] T. Wick, Coupling of fully Eulerian and arbitrary Lagrangian–Eulerian methods for fluid-structure interaction computations, Computational Mechanics 52 (5) (2013) 1113–1124. doi:10.1007/s00466-013-0866-3.

[20] S. Frei, Eulerian finite element methods for interface problems and fluid-structure interactions, Ph.D. thesis, Universitt Heidelberg (2016).

[21] S. Frei, T. Richter, A locally modified parametric finite element method for interface problems, SIAM Journal on Numerical Analysis 52 (5) (2014) 2315–2334.

[22] W. A. Wall, A. Gerstenberger, P. Gamnitzer, C. Forster, E. Ramm, Large deformation fluid-structure interaction-advances in ALE methods and new fixed grid approaches, Lecture Notes in Computational Science and Engineering 53 (2006) 195.

[23] Y. Sudhakar, J. M. De Almeida, W. A. Wall, An accurate, robust, and easy-to-implement method for integration over arbitrary polyhedra: application to embedded interface methods, Journal of Computational Physics 273 (2014) 393–415.

[24] D. Mitrovic, D. Zubrinic, Fundamentals of applied functional analysis, Vol. 91, CRC Press, 1997.

[25] S. Boyd, L. Vandenberghe, Convex optimization problems, in: Convex Optimization, Cambridge University Press, pp. 127–214. doi:10.1017/cbo9780511804441.005.
URL https://doi.org/10.1017%2Fcbo9780511804441.005

[26] O. Pironneau, Finite element methods for fluids, Wiley Chichester, 1989.

[27] O. Zienkiewic, The finite element method for fluid dynamics, 6th Edition, Elsevier BV, 2005.

[28] D. N. Arnold, F. Brezzi, B. Cockburn, L. D. Marini, Unified analysis of discontinuous Galerkin methods for elliptic problems, SIAM Journal on Numerical Analysis 39 (5) (2002) 1749–1779. doi:10.1137/s0036142901384162.

[29] D. Boffi, N. Cavallini, F. Gardini, L. Gastaldi, Local mass conservation of Stokes finite elements, Journal of Scientific Computing 52 (2) (2011) 383–400. doi:10.1007/s10915-011-9549-4.